The Astrophysical Journal, 838:11 (14pp), 2017 March 20 https://doi.org/10.3847/1538-4357/aa5be7

Nearest Neighbor: The Low-mass Milky Way Satellite Tucana III*

J. D. Simon[1], T. S. Li[2,3], A. Drlica-Wagner[2], K. Bechtol[4], J. L. Marshall[3], D. J. James[5,6], M. Y. Wang[3], L. Strigari[3], E. Balbinot[7], K. Kuehn[8], A. R. Walker[6], T. M. C. Abbott[6], S. Allam[2], J. Annis[2], A. Benoit-Lévy[9,10,11], D. Brooks[10], E. Buckley-Geer[2], D. L. Burke[12,13], A. Carnero Rosell[14,15], M. Carrasco Kind[16,17], J. Carretero[18,19], C. E. Cunha[12], C. B. D'Andrea[20,21], L. N. da Costa[14,15], D. L. DePoy[3], S. Desai[22], P. Doel[10], E. Fernandez[19], B. Flaugher[2], J. Frieman[2,23], J. García-Bellido[24], E. Gaztanaga[18], D. A. Goldstein[25,26], D. Gruen[12,13], G. Gutierrez[2], N. Kuropatkin[2], M. A. G. Maia[14,15], P. Martini[27,28], F. Menanteau[16,17], C. J. Miller[29,30], R. Miquel[31,19], E. Neilsen[2], B. Nord[2], R. Ogando[14,15], A. A. Plazas[32], A. K. Romer[33], E. S. Rykoff[12,13], E. Sanchez[24], B. Santiago[14,34], V. Scarpine[2], M. Schubnell[30], I. Sevilla-Noarbe[24], R. C. Smith[6], F. Sobreira[14,35], E. Suchyta[36], M. E. C. Swanson[17], G. Tarle[30], L. Whiteway[10], and B. Yanny[2]
(The DES Collaboration)

[1] Carnegie Observatories, 813 Santa Barbara Street, Pasadena, CA 91101, USA
[2] Fermi National Accelerator Laboratory, P.O. Box 500, Batavia, IL 60510, USA
[3] George P. and Cynthia Woods Mitchell Institute for Fundamental Physics and Astronomy, and Department of Physics and Astronomy, Texas A&M University, College Station, TX 77843, USA
[4] LSST, 933 North Cherry Avenue, Tucson, AZ 85721, USA
[5] Astronomy Department, University of Washington, Box 351580, Seattle, WA 98195, USA
[6] Cerro Tololo Inter-American Observatory, National Optical Astronomy Observatory, Casilla 603, La Serena, Chile
[7] Department of Physics, University of Surrey, Guildford GU2 7XH, UK
[8] Australian Astronomical Observatory, North Ryde, NSW 2113, Australia
[9] CNRS, UMR 7095, Institut d'Astrophysique de Paris, F-75014, Paris, France
[10] Department of Physics & Astronomy, University College London, Gower Street, London WC1E 6BT, UK
[11] Sorbonne Universités, UPMC Univ Paris 06, UMR 7095, Institut d'Astrophysique de Paris, F-75014, Paris, France
[12] Kavli Institute for Particle Astrophysics & Cosmology, P.O. Box 2450, Stanford University, Stanford, CA 94305, USA
[13] SLAC National Accelerator Laboratory, Menlo Park, CA 94025, USA
[14] Laboratório Interinstitucional de e-Astronomia—LIneA, Rua Gal. José Cristino 77, Rio de Janeiro, RJ—20921-400, Brazil
[15] Observatório Nacional, Rua Gal. José Cristino 77, Rio de Janeiro, RJ—20921-400, Brazil
[16] Department of Astronomy, University of Illinois, 1002 W. Green Street, Urbana, IL 61801, USA
[17] National Center for Supercomputing Applications, 1205 West Clark Street, Urbana, IL 61801, USA
[18] Institut de Ciències de l'Espai, IEEC-CSIC, Campus UAB, Carrer de Can Magrans, s/n, E-08193 Bellaterra, Barcelona, Spain
[19] Institut de Física d'Altes Energies (IFAE), The Barcelona Institute of Science and Technology, Campus UAB, E-08193 Bellaterra (Barcelona), Spain
[20] Institute of Cosmology & Gravitation, University of Portsmouth, Portsmouth PO1 3FX, UK
[21] School of Physics and Astronomy, University of Southampton, Southampton SO17 1BJ, UK
[22] Department of Physics, IIT Hyderabad, Kandi, Telangana 502285, India
[23] Kavli Institute for Cosmological Physics, University of Chicago, Chicago, IL 60637, USA
[24] Centro de Investigaciones Energéticas, Medioambientales y Tecnológicas (CIEMAT), Madrid, Spain
[25] Department of Astronomy, University of California, Berkeley, 501 Campbell Hall, Berkeley, CA 94720, USA
[26] Lawrence Berkeley National Laboratory, 1 Cyclotron Road, Berkeley, CA 94720, USA
[27] Center for Cosmology and Astro-Particle Physics, The Ohio State University, Columbus, OH 43210, USA
[28] Department of Astronomy, The Ohio State University, Columbus, OH 43210, USA
[29] Department of Astronomy, University of Michigan, Ann Arbor, MI 48109, USA
[30] Department of Physics, University of Michigan, Ann Arbor, MI 48109, USA
[31] Institució Catalana de Recerca i Estudis Avançats, E-08010 Barcelona, Spain
[32] Jet Propulsion Laboratory, California Institute of Technology, 4800 Oak Grove Dr., Pasadena, CA 91109, USA
[33] Department of Physics and Astronomy, Pevensey Building, University of Sussex, Brighton BN1 9QH, UK
[34] Instituto de Física, UFRGS, Caixa Postal 15051, Porto Alegre, RS—91501-970, Brazil
[35] Universidade Federal do ABC, Centro de Ciências Naturais e Humanas, Av. dos Estados, 5001, Santo André, SP, 09210-580, Brazil
[36] Computer Science and Mathematics Division, Oak Ridge National Laboratory, Oak Ridge, TN 37831, USA

Received 2016 October 17; revised 2017 January 4; accepted 2017 January 5; published 2017 March 17

Abstract

We present Magellan/IMACS spectroscopy of the recently discovered Milky Way satellite Tucana III (Tuc III). We identify 26 member stars in Tuc III from which we measure a mean radial velocity of $v_{\rm hel} = -102.3 \pm 0.4\,({\rm stat.}) \pm 2.0\,({\rm sys.})\,{\rm km\,s^{-1}}$, a velocity dispersion of $0.1^{+0.7}_{-0.1}\,{\rm km\,s^{-1}}$, and a mean metallicity of $[{\rm Fe/H}] = -2.42^{+0.07}_{-0.08}$. The upper limit on the velocity dispersion is $\sigma < 1.5\,{\rm km\,s^{-1}}$ at 95.5% confidence, and the corresponding upper limit on the mass within the half-light radius of Tuc III is $9.0 \times 10^4\,M_\odot$. We cannot rule out mass-to-light ratios as large as $240\,M_\odot/L_\odot$ for Tuc III, but much lower mass-to-light ratios that would leave the system baryon-dominated are also allowed. We measure an upper limit on the metallicity spread of the stars in Tuc III of 0.19 dex at 95.5% confidence. Tuc III has a smaller metallicity dispersion and likely a smaller velocity dispersion than any known dwarf galaxy, but a larger size and lower surface brightness than any known globular cluster. Its metallicity is also much lower than those of the clusters with similar luminosity. We therefore tentatively suggest that Tuc III is the tidally stripped remnant of a dark matter-dominated dwarf galaxy, but

* This paper includes data gathered with the 6.5 m Magellan Telescopes located at Las Campanas Observatory, Chile.

additional precise velocity and metallicity measurements will be necessary for a definitive classification. If Tuc III is indeed a dwarf galaxy, it is one of the closest external galaxies to the Sun. Because of its proximity, the most luminous stars in Tuc III are quite bright, including one star at $V = 15.7$ that is the brightest known member star of an ultra-faint satellite.

Key words: dark matter – galaxies: dwarf – galaxies: individual (Tucana III) – galaxies: stellar content – Local Group – stars: abundances

Supporting material: machine-readable table

1. Introduction

The discovery of Milky Way satellites in the last few years has reached an extremely rapid pace, with the total number of objects found since 2015 nearly matching the entire previously known population (Bechtol et al. 2015; Drlica-Wagner et al. 2015b, 2016; Kim & Jerjen 2015; Kim et al. 2015a, 2015b; Koposov et al. 2015a; Laevens et al. 2015a, 2015b; Martin et al. 2015; Torrealba et al. 2016a, 2016b). The photometric identification of these objects in the Dark Energy Survey (DES) and other large surveys has far outstripped the spectroscopic follow-up efforts needed to characterize them. Spectroscopic analyses are available for less than a third of the new satellites. The lack of information about the internal kinematics and chemical abundances of these systems greatly diminishes our ability to use them to study dark matter and early galaxy formation.

One of the most intriguing of the recently discovered systems is Tucana III (Drlica-Wagner et al. 2015b). At a distance of just 25 kpc, Tuc III is among the nearest dwarf galaxies and dwarf galaxy candidates to the Milky Way, slightly closer than Sagittarius (Hamanowicz et al. 2016) and Draco II (Laevens et al. 2015b) and perhaps just beyond Segue 1 (Belokurov et al. 2007). If its dark matter content is similar to that of other satellites with stellar masses of $\sim 10^3\,M_\odot$, such as Segue 1 and Coma Berenices (Simon & Geha 2007; Simon et al. 2011), it would be a very promising target for indirect dark matter detection experiments (e.g., Ackermann et al. 2015; MAGIC Collaboration 2016). Moreover, Drlica-Wagner et al. (2015b) showed that Tuc III is at the center of a pair of very low surface brightness linear features extending out to a radius of 2° (870 pc). These streams of stars are likely tidal tails from the pending destruction of the system, which would make Tuc III a prototype for the tidal disruption of the smallest galaxies.

In this paper, we present an initial spectroscopic study of Tuc III, identifying its brightest member stars and measuring its global properties. This work will set the stage for more detailed follow-up efforts, especially focused on the tidal tails, the dynamical state of the system, and its chemical abundance patterns. In Section 2, we describe the instrument configuration, target selection, observations, and data reduction. We present our measurements of the velocities and metallicities of stars in Tuc III in Section 3. In Section 4, we derive the physical properties of Tuc III and consider its nature and origin. We summarize our results and discuss our conclusions in Section 5.

2. Observations and Data Reduction

2.1. Spectrograph Setup and Summary of Observations

We observed Tuc III with the IMACS spectrograph (Dressler et al. 2006) on the Magellan Baade telescope on five nights in 2015 July, one night in 2015 October, and four nights in 2016 August/September. We used the $f/4$ camera on IMACS, which provides a 15.′4 square field of view for multi-slit spectroscopy. The $f/4$ camera uses a 4×2 array of 2048×4096 pixel e2v CCDs to create an 8192×8192 mosaic, with the spectral direction corresponding to the 2048 pixel axis of each detector. Our spectra were obtained with two gratings, both ruled at 1200 ℓ/mm but with different blaze angles. The new 1200/32.°7 grating acquired for this project reaches a peak throughput (including the spectrograph and the telescope) of 15.4% from 7800 to 8800 Å, while the pre-existing 1200/26.°7 grating peaks at 20% at 6500–7500 Å but has only 12% throughput at 8500 Å. Both gratings produce spectra at a resolution of $R \approx 11{,}000$ (for a 0.″7 slit) with a dispersion of 0.19 Å pix^{-1}. We observed with two spectrograph setups, one covering 7400–9000 Å targeting the Ca triplet (CaT) absorption lines (primarily with the 1200/32.°7 grating) and one covering 6300–7900 Å targeting Hα (primarily with the 1200/26.°7 grating). In order to cover these entire wavelength ranges, which include both strong stellar absorption features (CaT and Hα) and strong telluric absorption (Fraunhofer A-band) to provide a wavelength reference (e.g., Simon & Geha 2007; Sohn et al. 2007), the placement of slits is limited to a $15' \times 8'$ portion of the full field of view. All observations were obtained with a wide-band 5600–9200 Å filter to block second-order light.

Because the positions of spectral lines on the detector array are repeatable at the level of a few pixels rather than a fraction of a pixel as our velocity measurements require, we acquire calibration frames during the night. A typical observing sequence is to take several exposures of a slit mask lasting 1–1.5 hr, followed by exposures of comparison lamps and a flatfield lamp at the same position. Then the target is reacquired by taking a short exposure with the grating removed but the mask left in place. For observations obtained through 2015 October the comparison lamps were He, Ne, and Ar, but in later observing runs we replaced the He lamps with Kr lamps to provide additional useful calibration lines in the critical 7600–7900 Å wavelength range.

We observed a total of five slit masks targeting candidate member stars in Tuc III (see Section 2.2). Mask 1 contained 63 $0.''7 \times 5.''0$ slits and was observed in the CaT configuration for a total of 6.5 hr on the nights of 2015 July 16 and 17. The observing conditions on those nights were clear, with seeing ranging from 0.″8 to 1.″1. We also observed Mask 1 in the Hα configuration for a total of 7 hr on 2015 July 18 and 20, with partially cloudy conditions and seeing generally above 1″. Since the Hα spectroscopy was not planned as far in advance as would ideally be the case, we used the same mask rather than one designed for the required grating angle. While most targets were unaffected, the spectra from several slits fell partially off of the detector or overlapped with each other. Mask 2 contained 58 slits (including 41 new stars and 17 that were also on Mask 1) and was designed primarily to target a

Table 1
Observations

Mask Name	α (J2000) (h m s)	δ (J2000) (° ′ ″)	Slit PA (deg)	t_{exp} (s)	MJD of Observation[a]	# of Slits	% Useful Spectra
Mask 1	23 56 49.50	−59 34 40.0	292.0	23400	57220.8	63	54%
Mask 2	23 57 15.90	−59 34 34.0	172.0	3600	57223.3	58	17%
				2400	57312.2		36%
Long slit	23 55 23.60	−59 30 34.8	128.6	2700	57223.3	2	100%
Mask 3	23 56 48.00	−59 35 10.0	297.0	37200	57630.9	64	70%
Mask 4	23 58 20.00	−59 38 00.0	172.0	3600	57632.1	30	63%
Mask 5	23 55 13.00	−59 31 45.0	221.0	5400	57632.8	34	62%

Note.
[a] For observations made over multiple nights, the date listed here is the weighted mean observation date, which may occur during daylight hours.

few bright stars that could not be placed on Mask 1. Mask 2 was observed for 1.0 hr on 2015 July 19 in very poor conditions (1.″4 seeing) and for 0.67 hr on 2015 October 17 in better weather (0.″9 seeing). During the unusually bad seeing on 2015 July 19 we also observed two very bright stars (one of which did not fit on either slit mask) with a 0.″7-wide long slit for 0.75 hr.

For the 2016 observing run we designed three additional CaT slit masks targeting both member stars identified in 2015 observations and new member candidates. Mask 3 contained 64 slits, including most of the brighter confirmed members and a large sample of fainter candidates on the main sequence. We observed Mask 3 for a total of 10.3 hr on the nights of 2016 August 29 and 30 in good conditions with seeing mostly between 0.″5 and 0.″8. Masks 4 and 5 were designed to observe all remaining bright ($g < 20$) candidates within 15′ (2.5× the half-light radius) of the center of Tuc III. Mask 4 (with 30 stars) was observed for 1.0 hr on the night of 2016 August 31 in 0.″6–1.″0 seeing. Mask 5 (containing 34 stars) was observed for a total of 1.5 hr on 2016 August 31 and 2016 September 2 in 0.″7 seeing. The observations of each mask are summarized in Table 1.

2.2. Target Selection

We selected targets for spectroscopy using photometry from the DES Year 2 quick release (Y2Q1) catalog (Drlica-Wagner et al. 2015b). Guided by the colors of spectroscopically confirmed members of the DES-discovered dwarf galaxies Reticulum II and Horologium I from Simon et al. (2015) and Koposov et al. (2015b), we employed a selection window for red giant branch (RGB) stars bounded on the blue side by the fiducial sequence of the metal-poor globular cluster M92 from An et al. (2008), transformed to the DES photometric system, and bounded on the red side by a 12 Gyr, [Fe/H] = −2.2 theoretical isochrone from Bressan et al. (2012). These isochrones are overplotted on the color–magnitude diagram (CMD) of Tuc III in Figure 1(a). Potential subgiants were selected using a 0.05 mag wide window in $g - r$ around the Bressan et al. isochrone for $20 < g < 20.4$. We selected stars at and below the main sequence turnoff based on the photometric membership probabilities derived from the likelihood analysis of Drlica-Wagner et al. (2015b). While we did not identify any blue horizontal branch (HB) stars likely to be members of Tuc III, we also selected a handful of candidate red HB stars at $0.41 < g - r < 0.47$ and $17.4 < g < 17.7$.

Stars were placed on the slit masks according to their prioritization in the categories discussed above. The highest priority targets were those meeting our RGB selection. The next highest priorities were for stars just outside the RGB window, but within 0.02 mag in $g - r$ of either the M92 or Bressan et al. (2012) isochrones. Subgiants and then main-sequence stars with membership probabilities higher than 0.5 were the next two categories, followed by main-sequence candidates with membership probabilities between 0.1 and 0.5 and red HB candidates. Finally, any remaining mask space was filled by stars with photometry that made them unlikely to be members. Within each category, priorities were based on brightness and distance from the center of Tuc III.

2.3. Data Reduction

We reduced the IMACS spectra using the following set of procedures. First, we performed bias subtraction using row-by-row and column-by-column medians of the column and row bias sections, respectively. The $f/4$ detector array suffers from pattern noise with a peak-to-peak amplitude of six counts that significantly affects the spectra of the faintest sources. The pattern varies from one exposure to the next, but is identical on all eight CCDs for any given frame. We therefore constructed a template of the pattern by stacking the eight CCDs and setting each pixel in the template equal to an average of the two lowest observed values for that pixel. When there is a significant CCD area that is not covered by spectra this procedure cleanly reproduced the pattern, but for densely packed data, many pixels are covered by a spectrum on all eight CCDs. In that case, the template contains artifacts where bright lines or stellar continua overlap on all of the chips. We modeled these artifacts by collapsing the template in the x (dispersion) direction and smoothing it with a Gaussian kernel with a full-width at half-maximum of 15 pixels (1.″65). This smoothed profile was subtracted from each column of the original template to create the final template, which was then subtracted from the data.

The next stage of the data reduction relied on the Cosmos pipeline described by Dressler et al. (2011).[37] Cosmos uses the comparison lamp images and the coordinates of the slits to derive an approximate wavelength solution and a map of each slit across the detector array. We then cut out each slit on each chip into a separate FITS file.

[37] http://code.obs.carnegiescience.edu/cosmos

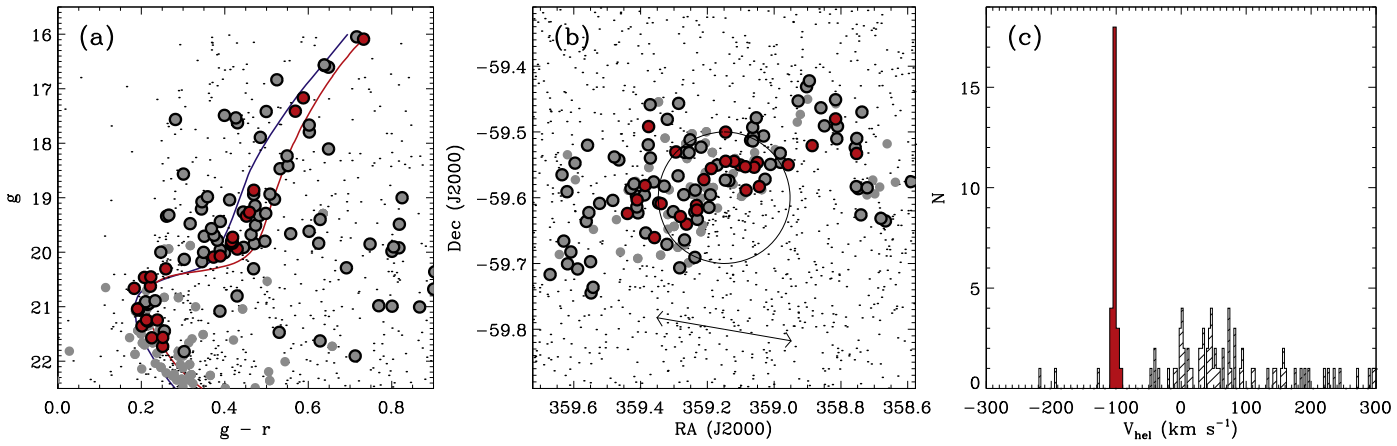

Figure 1. (a) DES color–magnitude diagram of Tucana III. Stars within 18′ of the center of Tuc III are plotted as small black dots and stars selected for spectroscopy (as described in Section 2.2) are plotted as filled gray circles. Points surrounded by black outlines represent the stars for which we obtained successful velocity measurements and those we identify as Tuc III members are filled in with red. The M92 sequence and PARSEC isochrone used to define the RGB of Tuc III are displayed as blue and red curves, respectively. (b) Spatial distribution of the observed stars. Symbols are as in panel (a). The arrow at the bottom illustrates the direction of the tidal tails identified by Drlica-Wagner et al. (2015b). These tidal tails make it difficult to determine the ellipticity of Tuc III with existing data, so we represent the half-light radius of Tuc III with a black circle. (c) Radial velocity distribution of observed stars. The clear narrow peak of stars at $v_{\rm hel} \sim -100$ km s^{-1} highlighted in red is the signature of Tuc III. The hatched histogram indicates stars that are not members of Tuc III.

From this point, we adapted the DEEP2 data reduction pipeline (Cooper et al. 2012; Newman et al. 2013) designed for the DEIMOS spectrograph at Keck to process IMACS data. The most significant difference between DEIMOS and IMACS spectra is that the IMACS spectrum of a single chip covers a much smaller wavelength range (∼390 Å rather than ∼1350 Å) because the spectra span the short axis of the 2048 × 4096 CCDs rather than the long axis and because of the smaller pixel scale. Deriving a wavelength solution accurate to better than 1 km s^{-1} is therefore more challenging because of the small number of arc lines per chip. In order to better constrain the problem, we constructed a single wavelength solution covering all four CCDs for each slit, fitting the positions of the arc lines with a third-order Legendre polynomial and leaving the widths of the three chip gaps spanned by each spectrum as free parameters. We then had a total of seven parameters (four polynomial coefficients and three chip gaps) to be determined from ∼35 arc lines, rather than determining four polynomial coefficients per chip from $\lesssim$9 lines. With the Cosmos wavelength solution providing an initial guess for this procedure, we achieved a typical rms of 0.35 km s^{-1} for 30–40 arc lines. The remainder of the DEEP2 pipeline, including flatfielding, sky subtraction, and extraction, required modifications primarily to handle the different format of the spectra and data files. All of the updates to DEIMOS reduction procedures described by Simon & Geha (2007) and Kirby et al. (2015b) have been retained in the IMACS version of the pipeline, with the exception of modifications related to differential atmospheric refraction because IMACS has an atmospheric dispersion corrector.

Each individual frame or set of frames was reduced and extracted using the corresponding calibration exposures. For the observations of Masks 1, 3, and 5 we then combined all of the extracted 1D spectra using inverse-variance weighting. Since the Mask 2 observations were obtained three months apart, radial velocity variations from binary orbital motion are possible (e.g., Koch et al. 2014), so we kept the July and October spectra separate.

3. Velocity and Metallicity Measurements

3.1. Radial Velocity Measurements

We measured radial velocities from the reduced spectra using the same procedures described by Simon & Geha (2007) and subsequent papers. We observed a set of bright, metal-poor stars in both IMACS configurations to provide radial velocity template spectra for χ^2 fitting. We also observed the hot, rapidly rotating star HR 4781 to serve as a telluric template. All of the template spectra were obtained by orienting the IMACS long slit north–south and driving the telescope in the R.A. direction such that the star moved at a constant rate across the slit during the exposure. These data thus provide a wavelength reference for a source that uniformly fills the slit. Integration times for the template observations were set at a minimum of 120 s so that night sky emission lines would be bright enough to check the wavelength solution from the comparison lamps. We reduced the template spectra as described in Section 2.3. The template spectra are normalized, with regions outside of telluric absorption bands set to unity for the telluric templates and regions inside the telluric bands set to unity for the velocity templates.

We measured the radial velocity of each science spectrum via χ^2 fits to the velocity templates (Simon & Geha 2007; Newman et al. 2013). For this paper we use the metal-poor subgiant HD 140283 (Fuhrmann et al. 1993) as the template for all of the science spectra. We assume a velocity of $v_{\rm hel} = -171.12$ km s^{-1} for this star (Latham et al. 2002). We determined a correction to the measured velocities to compensate for possible mis-centering of each star in its slit by fitting the A-band absorption of every spectrum with our telluric template. The A-band corrections are generally less than 6 km s^{-1}, but they show a systematic dependence on the position of the slit on the mask in the direction parallel to the slits. We modeled this dependence as a quadratic function, and for slits where an accurate correction could not be measured from the spectrum itself (either because of low S/N or because the telluric lines landed in a chip gap) we applied the model correction instead.

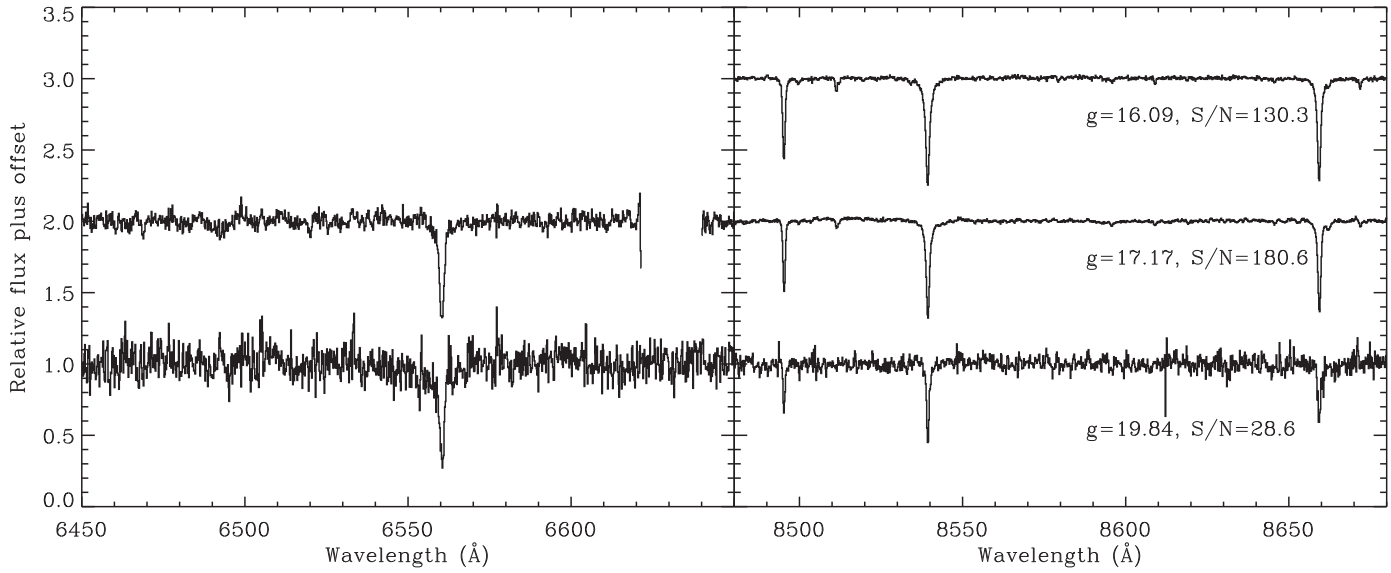

Figure 2. IMACS spectra of three Tuc III RGB stars. The Hα region of the spectrum is shown in the left panel, and the CaT region in the right panel. The top spectrum is DES J235532.66–593114.9, the brightest star in Tuc III, the middle spectrum is DES J235738.48–593611.6, a star ~1 mag fainter, and the bottom spectrum is DES J235655.47–593707.5, near the base of the RGB. The ~20 Å region with no data visible in the Hα spectrum of DES J235738.48–593611.6 is a gap between IMACS CCDs. Note that we did not obtain an Hα spectrum of DES J235532.66–593114.9.

As in Simon & Geha (2007), we calculated statistical uncertainties on each velocity measurement by performing Monte Carlo simulations in which normally distributed random noise is added to the observed spectrum and the template fitting is repeated. The uncertainty is defined to be the standard deviation of the Monte Carlo velocity measurements after $>5\sigma$ outliers have been rejected. Note that this procedure creates a Monte Carlo spectrum that is noisier than the actual data, and the uncertainty is therefore somewhat overestimated. For high S/N spectra the statistical uncertainty can be as small as 0.1 km s^{-1}, but that does not mean that the velocity measurements actually achieve that absolute accuracy. The process described above does not take into account the uncertainty in the wavelength solution (~0.35 km s^{-1}), the uncertainty of the A-band correction (~1 km s^{-1}), uncertainties in the template velocities, and other factors. In order to account for such possible systematic effects, we used stars that were observed on multiple nights to quantify the overall uncertainties on the velocity measurements. The systematic uncertainty varies slightly depending on which set of comparison lamps were used to determine the wavelength solution. For observations obtained with HeNeAr comparison lamps, we analyzed a sample of 62 stars with repeat measurements (including the Tuc III Mask 1 CaT observations as well as other data using the same spectrograph configuration) and found that we must add a systematic uncertainty of 1.2 km s^{-1} in quadrature with the statistical uncertainties to obtain a distribution of velocity differences that is consistent with the uncertainties (see Simon & Geha 2007; Simon et al. 2015). For observations obtained with KrNeAr lamps, the systematic uncertainty determined in the same manner is 1.0 km s^{-1} because of the improved wavelength solution on the blue end. IMACS is therefore able to reach better velocity accuracy than Keck/DEIMOS, likely thanks to its higher spectral resolution. We use 1.2 km s^{-1} (1.0 km s^{-1}) as the systematic uncertainty on the IMACS velocities obtained in 2015 (2016) for the remainder of this paper, with the reported velocity uncertainties being the quadrature sum of the statistical and systematic components. Combining the uncertainties in this way mitigates the overestimate of the statistical uncertainty mentioned above. All velocities presented here are in the heliocentric frame.

Because the velocity uncertainties derived from the Hα spectra are significantly larger than those determined from the CaT data, we do not use the Hα observations for any of the Tuc III measurements in this paper. They are used only for display purposes in Figure 2.

3.2. Metallicity Measurements

We measured metallicities for the red giant members of Tuc III based on the equivalent widths of the Ca triplet absorption lines. We follow the procedures described in Simon et al. (2015), fitting each of the three CaT lines with a Gaussian plus Lorentzian profile. We determine the equivalent width of each line by integrating the fitted Gaussian and Lorentzian functions. The statistical uncertainties on the equivalent widths are calculated from the uncertainties on the Gaussian and Lorentzian integrals. To convert the combined equivalent widths of the three lines to metallicity, we use the five-parameter CaT calibration of Carrera et al. (2013). As was the case for Reticulum II, Tuc III lacks known horizontal branch stars, so we rely on the CaT calibration with absolute V magnitude rather than the magnitude relative to the horizontal branch. We note that the faintest Tuc III RGB stars are located in a poorly constrained region of the Carrera et al. calibration, so it is possible that the metallicity uncertainties are larger than indicated for those stars. We determine a systematic uncertainty on the summed equivalent widths of the CaT lines using repeat measurements (in the same way as for the systematic uncertainty on the velocities in Section 3.1) of 0.32 Å. The statistical and systematic equivalent width uncertainties are added in quadrature. The dominant uncertainty on the derived metallicities comes from the combined statistical plus systematic measurement uncertainty of the CaT equivalent widths. For high S/N spectra the systematic uncertainty dominates, while for S/N $\lesssim$ 15 the statistical uncertainty is comparable or larger.

3.3. Spectroscopic Membership Determination

The CMD, spatial distribution, and velocity distribution of the observed stars are displayed in Figure 1. From the sample of stars with reliable velocity measurements (as determined by examination of the χ^2 fits to each spectrum), it is evident that Tuc III consists of stars in a narrow velocity range from $v_{\rm hel} = -95$ km s^{-1} to $v_{\rm hel} = -110$ km s^{-1}. The 26 stars selected with that velocity cut all lie exactly along the expected RGB-main-sequence track of Tuc III, and all have the spectra of old, metal-poor stars. We do not find any other stars within 25 km s^{-1} of this velocity, indicating that more sophisticated statistical methods to identify member stars are not necessary in this data set. We classify these 26 objects as Tuc III members and all other stars for which we are able to measure a velocity as non-members. Velocity measurements for all stars are listed in Table 2.

Despite its very low luminosity, Tuc III contains at least three relatively bright stars. The most luminous giant we have identified, DES J235532.66–593114.9, has a V magnitude of 15.7, ∼0.3 mag brighter than the brightest previously known star in an ultra-faint dwarf galaxy (Simon et al. 2015). This star and the next two brightest Tuc III members (which are both around 17th magnitude) will be outstanding targets for future chemical abundance studies based on high-resolution spectroscopy. Example spectra of three Tuc III members are displayed in Figure 2.

4. Discussion

In this section, we determine the global properties of Tuc III and then consider their implications for its nature and origin.

4.1. Velocity Dispersion and Mass

We determine the mean velocity and velocity dispersion of the Tuc III member stars using the Markov Chain Monte Carlo (MCMC) code `emcee`[38] (Foreman-Mackey et al. 2013) to maximize the Gaussian likelihood function defined by Walker et al. (2006). We find a systemic velocity of $v_{\rm hel} = -102.3 \pm 0.4$ (stat.) $\pm$ 2.0 (sys.) km s^{-1}, where the statistical uncertainty on the mean velocity corresponds to the 68% confidence interval and the systematic uncertainty results from the uncertainty on the velocity zero-point of the template star. We measure a velocity dispersion of $\sigma = 0.1^{+0.7}_{-0.1}$ km s^{-1}, where the uncertainties again represent the 68% confidence interval. The 90%, 95.5%, and 99.7% upper limits on the velocity dispersion are 1.2 km s^{-1}, 1.5 km s^{-1}, and 2.3 km s^{-1}, respectively. The only other known Milky Way satellite to have a comparably small dispersion is Segue 2 (Kirby et al. 2013a), for which the 90% (95%) upper limit is 2.2 km s^{-1} (2.6 km s^{-1}).

In general, it is possible that binary stars can affect velocity dispersion measurements for kinematically cold systems. Previous studies indicate that binary stars generally do not substantially inflate the observed velocity dispersions of ultra-faint dwarfs (Minor et al. 2010; Simon et al. 2011), but the smaller the dispersion of an object, the larger the impact of the binaries could be (McConnachie & Côté 2010). Approximate radial velocity amplitudes are only known for a handful of ultra-faint dwarf RGB binaries, but typical orbital velocities and periods appear to be ∼30 km s^{-1} and a few months, respectively (Koposov et al. 2011; Koch et al. 2014; Ji et al. 2016). We have obtained multiple velocity measurements spaced ∼1 year apart for 11 of the Tuc III member stars, including 8 of the 10 RGB stars, which have the smallest velocity uncertainties and are therefore the most important in determining the velocity dispersion. For 8 of the 11 stars with repeat measurements, the velocities agree within the 1σ uncertainties, and for the other 3, the velocity difference is between 1 and 1.5σ (see Table 2). These results are in accordance with expectations from Gaussian statistics if all of the stars have velocities that are constant with time. We conclude that there is no evidence that our Tuc III member sample contains any binaries with short enough periods or large enough amplitudes to affect our constraint on the velocity dispersion.

We use the upper limit on the velocity dispersion of Tuc III along with its half-light radius to constrain the mass contained within its half-light radius according to the formula derived by Wolf et al. (2010). Ignoring the uncertainty on the radius (which is only 14%; Drlica-Wagner et al. 2015b), we find 90%, 95.5%, and 99.7% upper limits of $M_{1/2} \leqslant 6.0 \times 10^4\,M_\odot$, $M_{1/2} \leqslant 9.0 \times 10^4\,M_\odot$, and $M_{1/2} \leqslant 2.2 \times 10^5\,M_\odot$, respectively. Given a luminosity within the same radius of 390 $L_\odot$, Tuc III could have a mass-to-light ratio as large as 240 $M_\odot/L_\odot$ at 2σ (or 580 $M_\odot/L_\odot$ at 3σ). The dynamical mass-to-light ratio would be larger than 10 as long as $M_{1/2} > 3900\ M_\odot$. Using the Wolf et al. relation, $M_{1/2}/L_{1/2} > 10$ implies $\sigma > 0.3$ km s^{-1}. Despite its very small velocity dispersion, Tuc III can easily be dynamically dominated by dark matter. However, firmly ruling out the alternative that Tuc III consists solely of baryons will only be possible with extremely accurate high-resolution spectroscopy of a significant sample of Tuc III stars.

Even though we are not able to directly measure the dynamical mass of Tuc III, we can estimate its mass via an indirect argument. Tuc III is currently located 23 kpc from the Galactic Center, and for a Galactic rotation velocity of 220 km s^{-1} (e.g., Bovy et al. 2012), the Milky Way mass enclosed out to that radius is $2.6 \times 10^{11}\,M_\odot$. The Jacobi (tidal) radius of Tuc III is therefore $r_J = 23000\,(M_{\rm Tuc\ III}/2.6 \times 10^{11}\,M_\odot)^{1/3}$ pc (Binney & Tremaine 2008). The 90%, 95.5%, and 99.7% upper limits on the Jacobi radius are then 142, 162, and 219 pc, respectively. The tidal tails of Tuc III are visible by a radius of 0.°3 (131 pc) and may extend inward as far as 0.°2 (87 pc), consistent with these upper limits. On the other hand, if Tuc III had a mass-to-light ratio of 1 $M_\odot/L_\odot$ ($M_{1/2} = 390\,M_\odot$), the Jacobi radius would be just 27 pc, which is not consistent with the observational result that the stars exhibit no detectable velocity gradient or dispersion out to a radius of ∼90 pc. If we demand based on the velocity data that $r_J > 90$ pc, the implied lower limit on the mass of Tuc III is $1.6 \times 10^4\,M_\odot$ (giving $M/L > 20\,M_\odot/L_\odot$).

N-body simulations suggest that the dynamical mass-to-light ratio of a dwarf galaxy is only modestly affected by tidal stripping until more than 90% of the original mass of the system has been lost (Peñarrubia et al. 2008). After that point, stripping actually increases the mass-to-light ratio because the central dark matter cusp is more tightly bound than the stars. The tidal tails around Tuc III have a similar luminosity to the bound core, suggesting that at least ∼50% of the stars initially in the system have been stripped. According to the Peñarrubia et al. models, the change in M/L with that amount of stripping is expected to be quite modest (∼30%). Interestingly, if Tuc III has suffered more significant stripping (in which case most of

[38] http://dan.iel.fm/emcee/current/

Table 2
Velocity and Metallicity Measurements for Tucana III

ID	MJD	R.A. (deg)	Decl. (deg)	g[a] (mag)	r[a] (mag)	S/N	v (km s^{-1})	EW (Å)	[Fe/H]	MEM
DES J235421.50−593432.2	57632.8	358.58958	−59.57561	19.32	19.05	6.5	10.66 ± 4.08	1.53 ± 0.43	…	0
DES J235440.00−593807.2	57632.8	358.66667	−59.63533	19.96	19.57	4.4	297.99 ± 7.77	…	…	0
DES J235443.22−593753.1	57632.8	358.68007	−59.63142	19.71	19.36	5.3	17.03 ± 2.74	4.88 ± 0.67	…	0
DES J235453.12−593505.3	57632.8	358.72131	−59.58481	18.47	17.93	21.3	10.54 ± 1.24	…	…	0
DES J235456.88−592811.2	57632.8	358.73701	−59.46979	17.79	17.19	48.9	77.36 ± 1.03	5.85 ± 0.34	…	0
DES J235457.61−593733.9	57632.8	358.74004	−59.62609	16.57	15.94	59.5	48.93 ± 1.04	6.13 ± 0.34	…	0
DES J235459.50−593510.4	57632.8	358.74790	−59.58622	21.52	20.60	3.2	82.51 ± 7.87	7.57 ± 1.29	…	0
DES J235500.62−593035.5	57632.8	358.75257	−59.50986	17.57	17.28	39.9	−1.04 ± 1.09	3.18 ± 0.43	…	0
DES J235500.75−593157.8	57632.8	358.75314	−59.53272	20.09	19.72	6.8	−103.30 ± 1.91	1.94 ± 0.47	…	1
DES J235500.98−593459.0	57632.8	358.75409	−59.58307	19.26	18.82	11.4	−40.92 ± 1.52	2.79 ± 0.50	…	0
DES J235501.69−593126.3	57632.8	358.75706	−59.52398	18.98	18.62	15.8	4.58 ± 1.30	3.31 ± 0.45	…	0
DES J235514.47−592929.2	57632.8	358.81029	−59.49145	19.91	19.47	10.8	−217.68 ± 1.71	5.53 ± 0.61	…	0
DES J235514.96−593037.6	57632.8	358.81232	−59.51044	21.63	21.00	3.0	−41.99 ± 11.23	…	…	0
DES J235515.82−592848.7	57632.8	358.81591	−59.48019	20.07	19.68	9.7	−102.39 ± 2.76	…	…	1
DES J235515.86−592703.6	57632.8	358.81608	−59.45100	20.98	20.21	6.6	90.16 ± 2.96	4.97 ± 1.11	…	0
DES J235523.86−592926.5	57632.8	358.84940	−59.49070	19.21	18.86	16.4	65.15 ± 1.31	2.05 ± 0.41	…	0
DES J235526.38−592747.9	57632.8	358.85993	−59.46330	19.78	19.40	11.3	2.62 ± 1.55	3.38 ± 0.55	…	0
DES J235532.66−593114.9	57223.3	358.88609	−59.52081	16.09	15.36	34.7	−102.32 ± 1.23	3.83 ± 0.35	−2.24 ± 0.15	1
	57632.8					130.2	−103.26 ± 1.00	3.57 ± 0.32	−2.35 ± 0.14	
DES J235534.70−592520.3	57632.8	358.89458	−59.42232	19.62	19.01	15.7	73.79 ± 2.06	5.24 ± 0.54	…	0
DES J235536.68−592552.4	57632.8	358.90281	−59.43122	21.90	21.19	3.0	74.31 ± 9.96	…	…	0
DES J235542.74−592710.6	57632.8	358.92807	−59.45293	18.57	18.27	22.6	51.17 ± 1.20	2.97 ± 0.38	…	0
DES J235549.90−593259.6	57220.8	358.95790	−59.54989	17.41	16.84	94.9	−102.88 ± 1.21	2.63 ± 0.33	−2.46 ± 0.17	1
	57223.3					7.2	−101.81 ± 2.90	2.29 ± 0.66	−2.63 ± 0.34	
	57630.9					142.6	−101.92 ± 1.00	2.66 ± 0.32	−2.45 ± 0.16	
DES J235555.49−593246.3	57220.8	358.98119	−59.54619	19.00	18.18	44.2	5.32 ± 1.24	5.93 ± 0.35	…	0
	57630.9					70.9	5.67 ± 1.02	5.90 ± 0.33	…	
DES J235555.60−593156.2	57220.8	358.98167	−59.53228	17.49	17.09	71.6	83.03 ± 1.22	4.83 ± 0.33	…	0
	57630.9					110.8	83.30 ± 1.01	5.12 ± 0.32	…	
DES J235602.62−593257.8	57220.8	359.01092	−59.54939	18.94	18.47	33.6	42.05 ± 1.27	3.83 ± 0.35	…	0
	57630.9					51.0	40.55 ± 1.02	4.19 ± 0.34	…	
DES J235606.52−593418.8	57220.8	359.02717	−59.57189	19.68	19.21	18.9	0.89 ± 1.51	5.46 ± 0.41	…	0
DES J235607.60−593022.1	57630.9	359.03166	−59.50614	21.03	20.05	19.2	158.96 ± 1.28	4.76 ± 0.45	…	0
DES J235610.63−593458.8	57630.9	359.04430	−59.58300	21.06	20.87	7.4	−103.72 ± 5.47	…	…	1
DES J235612.07−593247.5	57630.9	359.05029	−59.54653	21.56	21.31	4.4	−102.22 ± 5.48	…	…	1
DES J235612.82−592842.7	57630.9	359.05344	−59.47852	16.84	16.31	178.5	0.11 ± 1.00	6.24 ± 0.32	…	0
DES J235614.39−593313.2	57220.8	359.05997	−59.55368	20.62	20.40	5.6	−104.75 ± 2.61	…	…	1
	57630.9					11.0	−98.54 ± 3.98	…	…	
DES J235614.85−593022.1	57220.8	359.06186	−59.50613	19.85	19.10	23.1	43.88 ± 1.45	4.86 ± 0.44	…	0
	57630.9					38.2	43.36 ± 1.06	5.61 ± 0.36	…	
DES J235615.35−593049.8	57220.8	359.06397	−59.51384	19.44	19.05	19.7	103.70 ± 1.47	…	…	0
	57630.9					33.3	111.17 ± 1.17	4.53 ± 0.37	…	
DES J235615.42−592934.8	57220.8	359.06426	−59.49300	19.07	18.73	25.4	195.09 ± 1.33	5.05 ± 0.40	…	0
	57630.9					40.3	191.65 ± 1.08	…	…	
DES J235616.92−593045.5	57630.9	359.07051	−59.51263	20.96	20.74	7.3	63.29 ± 2.73	…	…	0
DES J235620.18−593518.8	57630.9	359.08409	−59.58857	21.73	21.48	4.2	−106.78 ± 3.23	1.20 ± 0.46	…	1
DES J235620.75−593310.1	57220.8	359.08645	−59.55279	18.86	18.39	30.6	−102.38 ± 1.27	2.23 ± 0.36	−2.36 ± 0.21	1
	57630.9					57.6	−102.82 ± 1.02	2.10 ± 0.34	−2.43 ± 0.20	
DES J235624.48−593300.4	57220.8	359.10202	−59.55010	20.46	20.25	7.0	−96.73 ± 9.11	…	…	1
	57630.9					12.0	−100.62 ± 2.04	1.19 ± 0.53	…	
DES J235628.83−593241.3	57220.8	359.12014	−59.54481	20.45	20.23	7.2	−101.57 ± 1.93	…	…	1
DES J235632.52−593427.1	57220.8	359.13552	−59.57420	20.17	19.83	10.0	165.35 ± 2.07	2.77 ± 0.73	…	0
	57630.9					17.2	160.84 ± 1.25	3.96 ± 0.52	…	
DES J235634.87−593001.1	57630.9	359.14530	−59.50029	21.27	21.05	5.6	−104.05 ± 4.12	…	…	1
DES J235634.88−593240.6	57630.9	359.14531	−59.54460	20.30	20.05	13.0	−100.81 ± 1.68	2.58 ± 0.46	…	1
DES J235635.09−593423.6	57220.8	359.14619	−59.57322	19.51	19.03	22.4	47.00 ± 1.38	4.74 ± 0.52	…	0
	57630.9					35.6	45.33 ± 1.07	5.30 ± 0.36	…	
DES J235640.91−593301.7	57220.8	359.17047	−59.55047	20.01	19.61	14.1	234.06 ± 5.87	…	…	0
DES J235645.16−593320.2	57630.9	359.18818	−59.55562	20.66	20.48	10.3	−105.69 ± 2.23	1.22 ± 0.49	…	1
DES J235645.76−593544.2	57630.9	359.19068	−59.59562	20.91	20.70	8.4	−127.83 ± 2.45	…	…	0
DES J235646.83−593652.8	57630.9	359.19511	−59.61467	20.89	20.66	8.8	355.50 ± 2.58	…	…	0
DES J235650.49−593420.9	57220.8	359.21037	−59.57247	19.94	19.51	14.1	−106.14 ± 1.55	2.14 ± 0.41	−2.19 ± 0.24	1
	57312.2					5.9	−103.48 ± 2.20	2.53 ± 0.76	−1.97 ± 0.41	

Table 2
(Continued)

ID	MJD	R.A. (deg)	Decl. (deg)	g[a] (mag)	r[a] (mag)	S/N	v (km s^{-1})	EW (Å)	[Fe/H]	MEM
	57630.9					27.2	−102.96 ± 1.12	1.66 ± 0.37	−2.49 ± 0.27	
DES J235652.54−593123.1	57220.8	359.21890	−59.52308	16.61	15.96	159.5	45.87 ± 1.20	6.04 ± 0.32	…	0
	57223.3					44.6	46.31 ± 1.24	6.34 ± 0.35	…	
	57312.2					56.7	45.81 ± 1.22	6.32 ± 0.34	…	
DES J235655.21−593758.0	57630.9	359.23003	−59.63278	20.36	19.46	33.8	158.24 ± 1.10	6.14 ± 0.38	…	0
DES J235655.47−593707.5	57220.8	359.23114	−59.61876	19.84	19.42	16.6	−104.40 ± 1.46	1.63 ± 0.34	−2.53 ± 0.25	1
	57312.2					6.3	−102.68 ± 3.12	1.45 ± 0.41	−2.66 ± 0.33	
	57630.9					28.6	−101.96 ± 1.12	1.56 ± 0.39	−2.58 ± 0.29	
DES J235655.78−593641.9	57630.9	359.23242	−59.61164	21.25	21.03	6.0	−108.37 ± 3.46	0.94 ± 0.42	…	1
DES J235656.72−593518.4	57220.8	359.23632	−59.58845	19.29	18.79	29.3	41.72 ± 1.34	5.13 ± 0.39	…	0
	57312.2					9.1	38.44 ± 1.85	7.40 ± 0.64	…	
DES J235656.95−594126.5	57223.3	359.23729	−59.69070	19.15	18.67	5.8	196.01 ± 2.42	2.37 ± 0.49	…	0
	57312.2					10.9	195.83 ± 1.75	2.93 ± 0.63	…	
DES J235657.00−593718.3	57220.8	359.23748	−59.62174	20.68	19.78	14.9	−32.76 ± 1.86	6.57 ± 0.47	…	0
	57312.2					5.5	−28.15 ± 2.81	7.53 ± 1.26	…	
	57630.9					26.5	−34.04 ± 1.21	6.65 ± 0.40	…	
DES J235700.42−593043.1	57312.2	359.25174	−59.51196	19.69	19.32	6.0	221.45 ± 6.06	…	…	0
DES J235701.15−593153.2	57220.8	359.25480	−59.53145	20.13	19.83	10.5	225.35 ± 2.60	4.66 ± 0.42	…	0
DES J235703.01−593824.6	57630.9	359.26254	−59.64017	21.57	21.34	5.2	−102.37 ± 6.41	…	…	1
DES J235704.33−593151.9	57220.8	359.26805	−59.53107	21.00	20.14	11.8	51.37 ± 2.24	4.49 ± 0.73	…	0
	57630.9					20.6	50.95 ± 1.52	6.72 ± 0.45	…	
DES J235704.40−593951.1	57312.2	359.26833	−59.66419	20.29	19.59	5.4	56.31 ± 3.12	…	…	0
DES J235704.96−593543.4	57220.8	359.27067	−59.59540	20.99	20.19	11.1	176.95 ± 1.92	4.45 ± 0.51	…	0
DES J235707.45−593742.9	57220.8	359.28106	−59.62858	19.73	19.31	18.4	−101.71 ± 1.55	1.32 ± 0.46	−2.78 ± 0.40	1
	57312.2					6.3	−101.93 ± 3.68	2.13 ± 0.60	−2.24 ± 0.35	
	57630.9					31.8	−102.90 ± 1.10	1.70 ± 0.34	−2.50 ± 0.24	
DES J235707.90−594223.7	57312.2	359.28293	−59.70660	20.16	19.20	8.3	−1.97 ± 2.43	7.13 ± 0.97	…	0
DES J235708.66−592723.5	57223.3	359.28609	−59.45652	18.11	17.46	15.9	31.59 ± 1.58	5.87 ± 0.51	…	0
	57312.2					21.4	29.55 ± 1.33	5.88 ± 0.43	…	
DES J235709.04−593400.3	57630.9	359.28767	−59.56675	21.82	21.52	3.9	−193.88 ± 7.22	…	…	0
DES J235710.69−593149.9	57630.9	359.29453	−59.53053	21.04	20.85	6.8	−103.03 ± 2.15	1.43 ± 0.43	…	1
DES J235712.50−593716.4	57220.8	359.30208	−59.62123	19.33	18.84	27.8	279.01 ± 1.32	4.63 ± 0.44	…	0
	57223.3					5.0	269.66 ± 4.31	…	…	
	57312.2					9.4	268.18 ± 1.65	4.46 ± 1.23	…	
	57630.9					45.5	272.18 ± 1.03	4.69 ± 0.34	…	
DES J235716.79−592851.0	57312.2	359.31996	−59.48085	19.98	19.18	7.7	112.22 ± 1.92	4.95 ± 0.93	…	0
DES J235717.09−594015.2	57223.3	359.32120	−59.67089	16.05	15.33	57.8	−46.26 ± 1.24	…	…	0
	57312.2					73.3	−44.85 ± 1.21	5.32 ± 0.34	…	
DES J235719.02−593456.6	57220.8	359.32925	−59.58239	17.63	17.20	83.7	45.36 ± 1.21	3.54 ± 0.33	…	0
DES J235721.26−593632.4	57630.9	359.33860	−59.60901	21.35	21.15	6.0	−94.60 ± 8.99	…	…	1
DES J235722.98−593628.5	57220.8	359.34576	−59.60793	19.84	19.21	21.6	29.07 ± 1.38	5.29 ± 0.60	…	0
	57630.9					36.4	27.96 ± 1.09	5.46 ± 0.36	…	
DES J235726.03−593938.1	57220.8	359.35845	−59.66059	19.27	18.81	24.4	−98.89 ± 1.35	1.66 ± 0.39	−2.62 ± 0.27	1
	57223.3					5.5	−99.65 ± 5.65	…	…	
	57312.2					9.7	−99.82 ± 1.80	2.44 ± 0.49	−2.16 ± 0.27	
	57630.9					41.7	−100.30 ± 1.06	2.12 ± 0.34	−2.34 ± 0.20	
DES J235726.62−593433.6	57630.9	359.36092	−59.57599	21.47	20.94	8.8	355.54 ± 1.88	5.22 ± 0.58	…	0
DES J235728.94−593222.6	57223.3	359.37059	−59.53962	19.04	18.63	5.9	80.31 ± 3.06	…	…	0
	57312.2					10.4	73.47 ± 1.66	4.50 ± 0.72	…	
DES J235729.11−592730.7	57223.3	359.37128	−59.45852	17.67	17.07	18.3	83.79 ± 1.49	6.94 ± 0.57	…	0
	57312.2					24.5	82.62 ± 1.31	6.32 ± 0.40	…	
DES J235730.23−592930.6	57312.2	359.37596	−59.49183	19.34	18.89	7.3	−99.51 ± 1.76	2.43 ± 0.70	−2.15 ± 0.38	1
DES J235730.51−593110.4	57312.2	359.37711	−59.51955	19.34	19.08	6.7	290.69 ± 2.40	5.70 ± 0.73	…	0
DES J235732.29−593913.0	57630.9	359.38452	−59.65360	20.94	20.72	6.6	−9.24 ± 1.92	…	…	0
DES J235732.74−593453.2	57630.9	359.38641	−59.58145	21.24	21.01	6.8	−106.67 ± 4.92	1.10 ± 0.48	…	1
DES J235733.29−593545.1	57220.8	359.38873	−59.59587	17.42	16.92	95.6	−2.55 ± 1.21	4.83 ± 0.33	…	0
	57223.3					21.6	−0.63 ± 1.37	5.34 ± 0.44	…	
	57312.2					31.1	−2.18 ± 1.28	5.47 ± 0.39	…	
	57630.9					143.0	−2.27 ± 1.00	5.32 ± 0.32	…	
DES J235737.91−593723.0	57630.9	359.40797	−59.62307	21.45	21.19	5.0	145.98 ± 2.26	4.05 ± 0.89	…	0
DES J235738.48−593611.6	57220.8	359.41034	−59.60323	17.17	16.58	120.5	−102.24 ± 1.21	2.46 ± 0.33	−2.60 ± 0.17	1
	57223.3					29.2	−100.30 ± 1.27	2.86 ± 0.35	−2.41 ± 0.17	
	57312.2					38.7	−102.37 ± 1.22	2.71 ± 0.35	−2.47 ± 0.17	

Table 2
(Continued)

ID	MJD	R.A. (deg)	Decl. (deg)	g[a] (mag)	r[a] (mag)	S/N	v (km s^{-1})	EW (Å)	[Fe/H]	MEM
	57630.9					180.6	−101.76 ± 1.00	2.72 ± 0.32	−2.47 ± 0.16	
DES J235738.70−593650.6	57220.8	359.41127	−59.61405	19.49	18.67	34.6	34.68 ± 1.25	5.33 ± 0.38	…	0
DES J235738.96−593549.9	57630.9	359.41235	−59.59721	19.48	19.16	32.4	−18.67 ± 1.11	5.43 ± 0.38	…	0
DES J235740.73−593444.4	57220.8	359.41969	−59.57901	17.54	17.11	83.2	33.40 ± 1.21	5.58 ± 0.33	…	0
	57630.9					130.6	32.25 ± 1.00	5.06 ± 0.32	…	
DES J235742.88−593509.4	57220.8	359.42866	−59.58596	18.93	18.43	38.1	95.94 ± 1.28	4.90 ± 0.36	…	0
DES J235745.45−593726.4	57632.1	359.43936	−59.62399	19.80	19.39	9.9	−99.34 ± 1.93	1.60 ± 0.40	−2.56 ± 0.29	1
DES J235751.61−593233.2	57632.1	359.46506	−59.54256	18.41	17.86	22.1	42.25 ± 1.26	5.56 ± 0.42	…	0
DES J235754.88−593217.1	57632.1	359.47868	−59.53808	17.89	17.41	26.2	33.66 ± 1.11	5.71 ± 0.38	…	0
DES J235755.96−593614.7	57632.1	359.48316	−59.60410	19.92	19.10	12.6	142.29 ± 1.46	7.05 ± 0.49	…	0
DES J235805.42−593630.9	57632.1	359.52258	−59.60860	19.66	19.10	11.1	−8.11 ± 1.51	4.90 ± 0.62	…	0
DES J235810.14−594410.4	57632.1	359.54225	−59.73623	19.86	19.44	8.3	183.36 ± 2.05	4.63 ± 0.78	…	0
DES J235811.57−594441.3	57632.1	359.54819	−59.74481	20.30	19.84	6.3	132.96 ± 2.18	2.49 ± 0.42	…	0
DES J235811.96−594150.0	57632.1	359.54984	−59.69723	20.00	19.75	6.2	243.32 ± 2.69	…	…	0
DES J235813.15−593721.4	57632.1	359.55478	−59.62260	19.90	19.10	12.1	59.45 ± 1.61	4.57 ± 0.53	…	0
DES J235814.12−593112.7	57632.1	359.55884	−59.52019	20.00	19.65	3.9	155.66 ± 4.23	3.85 ± 0.80	…	0
DES J235815.00−593809.9	57632.1	359.56251	−59.63607	21.08	20.69	2.5	2.37 ± 4.82	…	…	0
DES J235821.27−594229.9	57632.1	359.58862	−59.70831	20.80	20.37	4.1	14.22 ± 3.78	2.68 ± 0.67	…	0
DES J235823.12−593250.7	57632.1	359.59634	−59.54740	19.03	18.51	11.4	73.69 ± 1.75	5.98 ± 0.67	…	0
DES J235826.09−594056.8	57632.1	359.60869	−59.68245	19.80	19.30	9.1	45.45 ± 1.79	4.40 ± 0.65	…	0
DES J235828.48−594201.9	57632.1	359.61866	−59.70052	16.56	15.92	75.3	30.95 ± 1.01	5.87 ± 0.33	…	0
DES J235828.88−593527.0	57632.1	359.62035	−59.59082	19.40	18.77	13.9	42.48 ± 1.68	5.78 ± 0.62	…	0
DES J235831.24−593957.3	57632.1	359.63018	−59.66592	19.84	19.37	8.4	294.87 ± 1.40	…	…	0
DES J235832.47−593354.4	57632.1	359.63529	−59.56511	18.23	17.68	19.9	95.50 ± 1.27	6.13 ± 0.43	…	0
DES J235841.01−594300.3	57632.1	359.67088	−59.71676	19.57	19.20	9.4	35.42 ± 1.88	5.25 ± 0.59	…	0

Note. Some stars have multiple measurements made on different dates. These repeated measurements have been used to quantify systematic uncertainties (see Sections 3.1 and 3.2).
[a] Quoted magnitudes represent the weighted-average dereddened PSF magnitude derived from the DES images using SExtractor (Drlica-Wagner et al. 2015b).
(This table is available in machine-readable form.)

the stars must be in a more diffuse component of the tails that is below current detection limits), its unusually low velocity dispersion makes it consistent with a $10^6\ L_\odot$ progenitor with a 10 km s^{-1} velocity dispersion (Peñarrubia et al. 2008), similar to the classical dwarf spheroidals. However, its metallicity is lower than would be expected for such a large dwarf (see Section 4.2). The larger velocity dispersions of most other ultra-faint dwarfs are not consistent with the tidal evolution of more luminous systems.

4.2. Metallicity and Metallicity Spread

As seen in Figure 1, 10 of the Tuc III member stars in our sample are on the RGB, with the remainder of the sample on the subgiant branch or the main sequence. We measure CaT metallicities for the RGB members of Tuc III, which range from [Fe/H] = −2.16 to [Fe/H] = −2.58. Using the same MCMC method as in Section 4.1, we calculate a mean metallicity of $[\mathrm{Fe/H}] = -2.42^{+0.07}_{-0.08}$, with a dispersion of $\sigma_{[\mathrm{Fe/H}]} = 0.01^{+0.09}_{-0.01}$. The metallicity spread in Tuc III is therefore unresolved in these data, with an upper limit of 0.19 dex at 95.5% confidence. The posterior probability distributions from the MCMC fit are displayed in the right panel of Figure 3 and the kinematic and chemical properties of Tuc III are summarized in Table 3.

The metallicity range of the confirmed Tuc III members is smaller than that of other dwarf galaxies, especially those with similar luminosities (Kirby et al. 2013b). Other systems with $L < 10^4\ L_\odot$ such as Segue 2, Coma Berenices, and Ursa Major II have metallicity spreads of ∼0.4–0.6 dex, although some of those dwarfs also have larger samples of stars from which the spread can be measured. At 95.5% confidence we cannot rule out a spread of ∼0.2 dex in Tuc III, so given the currently available data we conclude that the apparently narrow metallicity range of Tuc III stars is most likely a coincidence resulting from the small sample size. If this result persists with a larger member sample or with more accurate measurements then other hypotheses may need to be considered.

4.3. The Nature of Tucana III

Willman & Strader (2012) suggested that a stellar system could be classified as a galaxy if it has either dynamical evidence for the presence of dark matter or chemical evidence for the retention of supernova ejecta. This chemical evidence would consist of an internal spread in the abundance of iron or other heavy elements formed only in explosive events. Unfortunately, since we are only able to place upper limits on the dynamical mass and metallicity spread, we cannot classify Tuc III with these standard criteria.

The stellar kinematics of Tuc III (Section 4.1) are consistent either with a dark matter-dominated system if $\sigma \gtrsim 0.3$ km s^{-1} or a baryon-dominated one if $\sigma \lesssim 0.3$ km s^{-1}. Tuc III therefore cannot be robustly classified based on its kinematics. Even if the velocity dispersion is near the upper limits we derive, it is worth noting that recent numerical simulations of disrupting

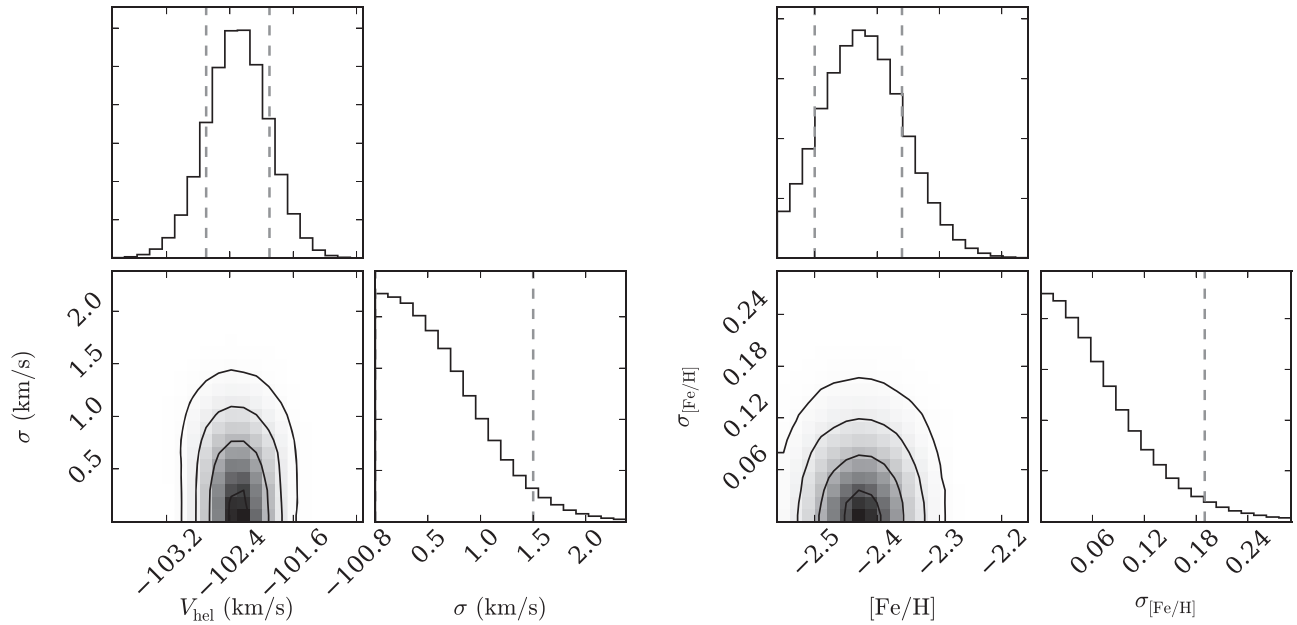

Figure 3. Posterior probability distribution from a maximum-likelihood fit for the systemic velocity and velocity dispersion (left set of panels) and the mean metallicity and metallicity dispersion (right set of panels) of Tuc III. In the upper left panels the 68% confidence intervals on the mean velocity and metallicity are indicated by the dashed gray lines. In the lower right panels the 95.5% upper limits on the velocity and metallicity dispersion are indicated by the dashed gray lines. We do not significantly resolve either the velocity dispersion or the metallicity dispersion of Tuc III.

Table 3
Summary of Properties of Tucana III

Row	Quantity	Value
(1)	R.A. (J2000)	23:56:36
(2)	Decl. (J2000)	−59:36:00
(3)	Distance (kpc)	25 ± 2
(4)	$M_{V,0}$	−2.4 ± 0.4
(5)	$L_{V,0}$ ($L_\odot$)	780^{+350}_{-240}
(6)	$r_{1/2}$ (pc)	44 ± 6
(7)	$V_{\rm hel}$ (km s^{-1})	−102.3 ± 0.4 ± 2.0
(8)	$V_{\rm GSR}$ (km s^{-1})	−195.2 ± 0.4 ± 2.0
(9)	σ (km s^{-1})[a]	<1.5
(10)	Mass ($M_\odot$)[a]	<8 × 10^4
(11)	M/L_V ($M_\odot/L_\odot$)[a]	<240
(12)	Mean [Fe/H]	$-2.42^{+0.07}_{-0.08}$
(13)	Metallicity dispersion (dex)[a]	<0.19
(14)	$\log_{10} J$ (0.°2) (GeV^2 cm^{-5})	<17.8

Note. Rows (1)–(6) are taken from the DES photometric analysis of Drlica-Wagner et al. (2015b). Values in rows (7)–(14) are derived in this paper.
[a] Upper limits listed here are at 95.5% confidence. See the text for values at other confidence levels.

clusters suggest that they can briefly reach velocity dispersions of ∼1.5 km s^{-1} and half-light radii above 20 pc just before complete disruption occurs (Contenta et al. 2017).

The metallicity spread within Tuc III (Section 4.2) is also consistent with either a dark matter-dominated dwarf galaxy or a baryon-dominated cluster. Its metallicity spread appears to be smaller than those of other low-luminosity dwarfs, but with only CaT-based metallicities and our limited sample of stars we cannot rule out a substantial spread in [Fe/H].

Given the lack of detection of a velocity or metallicity dispersion, we instead attempt to classify Tuc III using some of its other properties. The low mean metallicity of Tuc III suggests that it is not a globular cluster (Figure 4, left panel). Among known globular clusters, only the much more luminous clusters M15 (Preston et al. 2006; Sobeck et al. 2011) and M92 (Roederer & Sneden 2011) have comparable or lower metallicities. Considering just the low-luminosity ($M_V > -5$) clusters, the mean metallicity of the objects in the 2010 edition of the Harris (1996) catalog is [Fe/H] = −1.1 and the lowest-metallicity system is Palomar 13, listed at [Fe/H] = −1.88. The only high-resolution abundance measurement for Pal 13 is that of Côté et al. (2002), who found [Fe/H] = −1.98 ± 0.31 for the brightest star. Correcting that metallicity to a modern value for the solar iron abundance would increase it to [Fe/H] = −1.81. Bradford et al. (2011) determined a slightly higher value of [Fe/H] = −1.6 from spectral synthesis modeling of medium-resolution spectra. The metallicity of Tuc III would make it a significant outlier among low-luminosity clusters. In contrast, the low metallicity of Tuc III fits naturally in the context of ultra-faint dwarf galaxies. The metallicity predicted for its luminosity from the universal luminosity–metallicity relation of Kirby et al. (2013b) is [Fe/H] = −2.58. Tuc III is slightly, although not significantly, above the relation, consistent with the idea that what we are observing today is the remnant of a system that used to be more luminous. Placing Tuc III exactly on the luminosity–metallicity relation would result in a luminosity of 2600 $L_\odot$, implying that ∼70% of Tuc III's stars may have been removed by tidal stripping.

Another diagnostic that can be used to distinguish dwarf galaxies from globular clusters is size: it has been known for many years that globular clusters have smaller radii than dwarfs at the same luminosity (e.g., Belokurov et al. 2007). A half-light radius of 44 ± 6 pc and corresponding surface brightness of 28.7 mag arcsec^{-2} places Tuc III firmly within the dwarf galaxy locus, more extended than the similarly faint dwarfs Segue 1, Willman 1, Segue 2, and Triangulum II, as well as all low-luminosity globular clusters (Figure 4, upper left panel). Unless the size of Tuc III has been significantly inflated as a

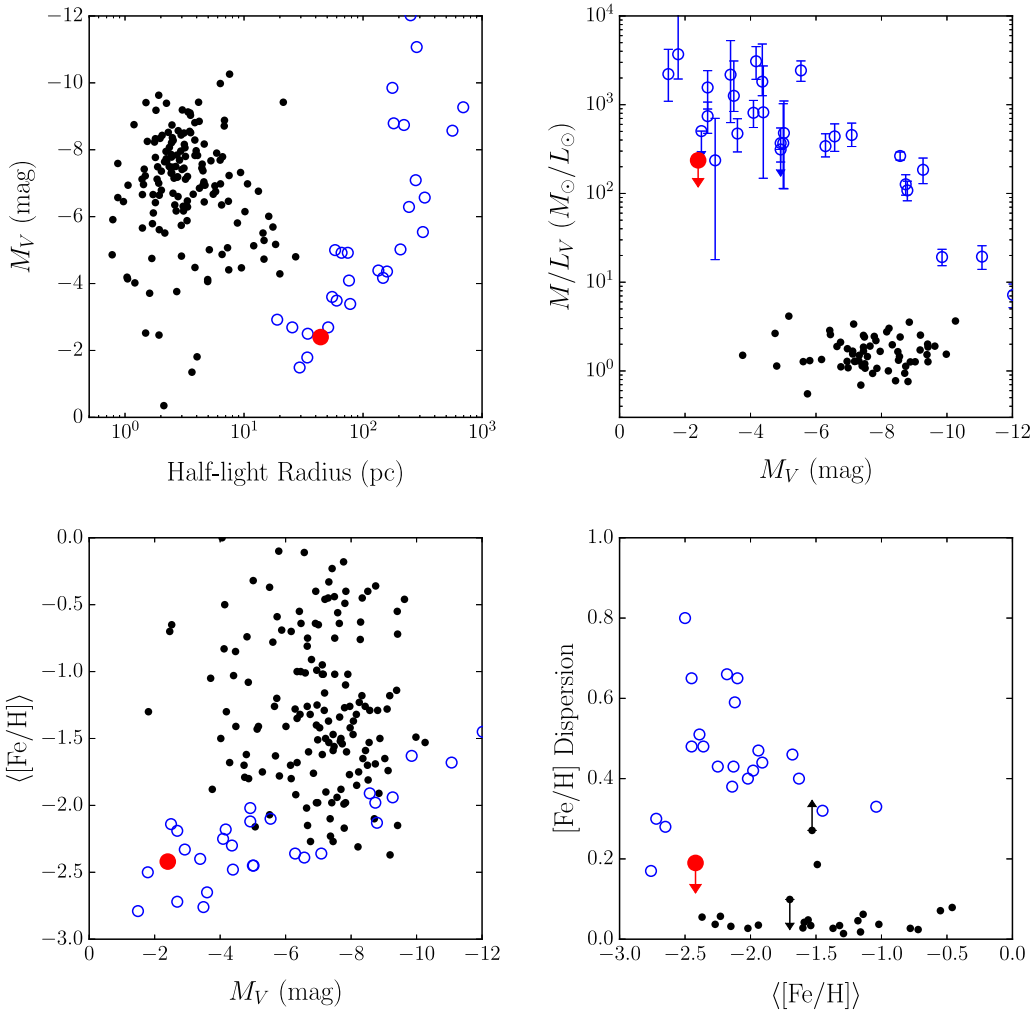

Figure 4. Position of Tuc III relative to dwarf galaxy scaling relations. (upper left) Distribution of Milky Way globular clusters (small filled black points) and spectroscopically confirmed Milky Way satellite galaxies (open blue circles) in the plane of elliptical half-light radius and absolute magnitude. Tuc III is plotted as a filled red circle. (upper right) Dynamical mass-to-light ratios for dwarf galaxies and globular clusters as a function of absolute magnitude. Masses shown are calculated as the mass within the elliptical half-light radius using the formula from Wolf et al. (2010). Symbols are as in the upper left panel, except that Tuc III and Segue 2 are plotted as upper limits. (lower left) The luminosity–metallicity relation for dwarf galaxies and lack thereof for globular clusters. Symbols are the same as in the upper left panel. (lower right) Metallicity dispersion as a function of metallicity for dwarf galaxies and globular clusters. Symbols are the same as in the upper left panel. The globular cluster data shown in this figure are taken from the 2010 edition of the Harris (1996) catalog, with the exception of the metallicity dispersions, which are from Willman & Strader (2012) and references therein. Half-light radii of the dwarf galaxies are taken from the 2015 September update of the McConnachie (2012) compilation, while velocity dispersions are taken from McConnachie (2012) for classical dSphs and otherwise from Simon & Geha (2007), Simon et al. (2011), Willman et al. (2011), Koposov et al. (2011, 2015b), Kirby et al. (2013a, 2015a, 2015b), Simon et al. (2015), Martin et al. (2016), Kim et al. (2016), Collins et al. (2017), Li et al. (2016b), and M. Geha et al. (2017, in preparation). Dwarf galaxy metallicities and metallicity dispersions are from Kirby et al. (2013b), the velocity dispersion references just listed, and Frebel et al. (2014), Brown et al. (2014), and Koch & Rich (2014).

result of tidal stripping, which is contrary to expectations from numerical simulations (Peñarrubia et al. 2008), its radius alone strongly suggests that it is a galaxy.

The shape of Tuc III is also more consistent with the population of faint dwarf galaxies than globular clusters. While Drlica-Wagner et al. (2015b) were not able to constrain its shape photometrically because of the extension of the tidal tails to relatively small radii, our spectroscopic member sample strongly suggests that Tuc III is highly elongated (see Figure 1(b)). One might assume that this shape is a result of our lack of spectroscopic coverage in the southwest portion of Tuc III (Figure 1(b)), but in fact the reason we did not observe that area is that we found no photometric RGB candidates there. As first noted by Martin et al. (2008), ultra-faint dwarfs have systematically larger ellipticities than both brighter dwarfs and globular clusters. It is widely assumed that very elongated shapes are a telltale sign of tidal disruption, but both simulations (Muñoz et al. 2008) and observations (e.g., Pal 5; Martin et al. 2008) argue to the contrary. Nevertheless, some disrupting systems are quite elliptical (such as Sagittarius), and it is possible that the shape of Tuc III is more closely related to its dynamical state than to its nature.

While the arguments presented here are not definitive, the combination of its low mean metallicity and structure and the difficulty of reconciling the lack of a velocity dispersion or gradient with tidal disruption inside the observed region indicates that Tuc III is most likely a dwarf galaxy rather than a globular cluster. This classification can be confirmed by much more accurate ($\sim$0.1 km s^{-1}) radial velocity measurements or by additional and/or more accurate metallicities demonstrating the existence of a spread of iron abundances.

If Tuc III is not a cluster, a possible explanation for its apparently very small metallicity spread is the tidal stripping the system has suffered. Several known dwarfs have been found to contain multiple stellar populations, with the metal-rich stars being centrally concentrated and the metal-poor ones more spatially extended (e.g., Tolstoy et al. 2004; Faria et al. 2007; Battaglia et al. 2011; de Boer et al. 2011; Santana et al. 2016). If the same were true for Tuc III then the metal-poor stars would be more likely to be stripped, increasing the mean metallicity and decreasing the metallicity dispersion of the remnant core of the system. Thus, while we would generally expect Tuc III to have a significant metallicity dispersion if it is a dwarf galaxy, the observed small dispersion is not necessarily inconsistent with a galactic classification if tidal stripping has altered the original metallicity distribution. This scenario can be tested by determining the metallicity of stars in the tidal tails.

Under the assumption that Tuc III is indeed a galaxy, it is one of the closest known dwarfs to the Sun. Until the recent flood of discoveries, the nearest dwarfs were Segue 1, at $d = 23 \pm 2$ kpc (Belokurov et al. 2007), and the Sagittarius dSph, at $d = 26.7 \pm 1.3$ kpc (Hamanowicz et al. 2016). The maximum-likelihood fit to the DES photometry by Drlica-Wagner et al. (2015b) places Tuc III in between the two, at $d = 25 \pm 2$ kpc, but a direct comparison of the Segue 1 and Tuc III CMDs suggests that the distances are indistiguishable without deeper photometry. Draco II, whose classification is unclear (Martin et al. 2016), is also at a similar distance from the Sun ($d = 24$ kpc; Laevens et al. 2015b). Of these objects, only Sagittarius is closer to the Galactic Center than Tuc III, so it is perhaps not surprising that those are the two satellites with the clearest signs of tidal disruption.

4.4. Constraints On the Orbit of Tuc III

The Galactocentric velocity that we measure for Tuc III is $v_{\rm GSR} = -195.2 \pm 0.4 \pm 2.0\,{\rm km\,s^{-1}}$. The large absolute value of the velocity suggests that we are observing Tuc III relatively close to the pericenter of its orbit around the Milky Way. Possible orbital configurations that would result in a negative radial velocity include (1) the pericenter is on the near side of the Galaxy relative to the Sun, with Tuc III currently approaching pericenter, (2) the pericenter is on the far side of the Galaxy and Tuc III is approaching pericenter, or (3) the pericenter is on the far side of the Galaxy and Tuc III has just passed pericenter. However, given the position of Tuc III ($\ell = 315\overset{\circ}{.}38$, $b = -56\overset{\circ}{.}19$ in Galactic coordinates), this last configuration requires a substantial tangential velocity for Tuc III, which would result in a very high space velocity. Without a proper motion for the system we cannot currently distinguish between these geometries, although radial velocity measurements in the tidal tails could provide additional constraints.

Our conclusion that Tuc III is near the pericenter of its orbit disagrees with the hypothesis of Drlica-Wagner et al. (2015b) that the short apparent length of the tidal tails suggests that Tuc III is near its orbital apocenter. The most obvious way to reconcile the velocity of Tuc III with the extent of the tails (viewed in projection) is if the tails are oriented such that they extend mostly along the line of sight, implying that the motion of Tuc III is also directed along the line of sight. In principle, a significant line-of-sight depth for the tails should be detectable photometrically, but the currently available data are not sufficient to constrain this possibility.

The observed velocity of Tuc III differs from the predictions of Jethwa et al. (2016) assuming that Tuc III is a satellite of the Magellanic Clouds. The heliocentric velocity of Tuc III differs by 150 km s^{-1} from that predicted for an LMC satellite and by 380 km s^{-1} from the prediction for an SMC satellite. However, the large uncertainties on the predictions of Jethwa et al. mean that the observed heliocentric velocity of Tuc III lies just outside the 68% confidence interval for being a satellite of the LMC. We therefore find that Tuc III is unlikely to be a satellite of the SMC or LMC, but that we cannot rule out these scenarios with high confidence. Consistent with this result, Sales et al. (2017) find that the position and distance of Tuc III give it a low probability of being associated with the LMC.

4.5. J-factor

We derive an astrophysical J-factor for dark matter annihilation by modeling the velocity distribution using the spherical Jeans equation (e.g., Strigari et al. 2008; Essig et al. 2009; Charbonnier et al. 2011; Martinez 2013; Geringer-Sameth et al. 2015; Simon et al. 2015). Here, we model the dark matter halo as a generalized Navarro–Frenk–White profile (Navarro et al. 1996). We use flat, "uninformative" priors on the dark matter halo parameters (see Essig et al. 2009) and assume a constant stellar velocity anisotropy and a tidal radius of 100 pc. From this procedure, we find an upper limit on the J-factor for Tuc III of $\log_{10}(J) < 17.8$ at 90% confidence within an angular cone of radius $0\overset{\circ}{.}2$. However, if we adopt the lower limit on the mass of Tuc III from the tidal radius argument in Section 4.1, J-factors as large as $\log_{10}(J) = 19.4$ are allowed. Because the tidal tails of Tuc III indicate that its dark matter halo is truncated at a radius of less than $0\overset{\circ}{.}5$ (see Section 4.1) we do not calculate J-factors for larger angular extents.

The upper limit on the J-factor of Tuc III is more than an order of magnitude below the value predicted from a simple distance scaling based on the J-factors of known dwarfs (e.g., Drlica-Wagner et al. 2015a). This low J-factor is a direct result of the small velocity dispersion and mass of Tuc III, which are both lower than would be expected from simple scaling relations. Thus, in spite of its proximity, Tuc III does not appear to be a particularly promising target for indirect searches for dark matter annihilation. While possible weak gamma-ray signals near Tuc III have been detected by Albert et al. (2016) and Li et al. (2016a), the low mass and J-factor of Tuc III suggest that this emission, if real, is probably not related to dark matter annihilation in Tuc III.

5. Summary and Conclusions

We obtained medium-resolution Magellan/IMACS spectroscopy of stars in the recently discovered Milky Way satellite Tucana III. By extending techniques developed for Keck/DEIMOS observations of similar systems, we show that it is possible to measure velocities with an accuracy of $\sim$1 km s^{-1} with the IMACS 1200 ℓ/mm grating. Based on extensive radial velocity measurements in the vicinity of Tuc III we identify 26 stars as Tuc III members, including 10 stars on the RGB. The brightest several member stars are well within range for high-resolution spectroscopy to determine chemical abundances, and the most luminous star in Tuc III

($V = 15.7$) is currently the brightest known star in an ultra-faint dwarf galaxy.

We find a mean velocity for Tuc III of $v_{\rm hel} = -102.3 \pm 0.4\,({\rm stat.}) \pm 2.0\,({\rm sys.})\,{\rm km\,s^{-1}}$ ($v_{\rm GSR} = -195.2 \pm 0.4 \pm 2.0\,{\rm km\,s^{-1}}$) and a velocity dispersion of $0.1^{+0.7}_{-0.1}\,{\rm km\,s^{-1}}$. The 95.5% and 99.7% confidence upper limits on the velocity dispersion are 1.5 km s^{-1} and 2.3 km s^{-1}, respectively. The mass within the half-light radius of Tuc III is therefore less than $9 \times 10^4\ M_\odot$ at 95.5% confidence, corresponding to an upper limit on the dynamical mass-to-light ratio of 240 $M_\odot/L_\odot$. Among ultra-faint stellar systems for which kinematic measurements are available, only Segue 2 ($\sigma < 2.2\,{\rm km\,s^{-1}}$ at 90% confidence; Kirby et al. 2013a) has a comparably small velocity dispersion.

Tuc III has a mean metallicity of $[{\rm Fe/H}] = -2.42^{+0.07}_{-0.08}$, with an unresolved spread of $\sigma_{\rm [Fe/H]} < 0.19$ dex at 95.5% confidence. We conclude that the low metallicity, large radius, elongated shape, and lack of detectable kinematic disturbances out to a radius of ~90 pc are most consistent with a dwarf galaxy classification for Tuc III, with a small residual dark matter component. Tuc III is therefore one of the closest dwarfs to the Sun. The placement of Tuc III relative to the luminosity–metallicity relation and its small metallicity dispersion may be the result of extensive tidal stripping. If interpreted instead as a globular cluster, it would be the most extended cluster known, with a metallicity $\gtrsim$0.5 dex lower than any similar-luminosity cluster. Further metallicity measurements to determine the iron abundance spread or detailed chemical abundance patterns for the brightest member stars can definitively confirm our classification.

The large negative velocity of Tuc III suggests that it is currently close to the pericenter of its orbit around the Milky Way. This velocity is quite different from that expected if Tuc III originated as a Magellanic satellite that has been accreted by the Milky Way, so we conclude that Tuc III probably did not form in the Magellanic group. Measurements of the proper motion of Tuc III and the velocity gradient in its tidal tails will constrain its orbit more tightly and firmly determine its origin.

This publication is based upon work supported by the National Science Foundation under grant AST-1108811. We thank Dan Kelson for many helpful conversations regarding IMACS data reduction and the anonymous referee for suggestions that improved the paper. E.B. acknowledges financial support from the European Research Council (ERC-StG-335936). This research has made use of NASA's Astrophysics Data System Bibliographic Services. Contour plots were generated using `corner.py` (Foreman-Mackey 2016).

Funding for the DES Projects has been provided by the U.S. Department of Energy, the U.S. National Science Foundation, the Ministry of Science and Education of Spain, the Science and Technology Facilities Council of the United Kingdom, the Higher Education Funding Council for England, the National Center for Supercomputing Applications at the University of Illinois at Urbana-Champaign, the Kavli Institute of Cosmological Physics at the University of Chicago, Financiadora de Estudos e Projetos, Fundação Carlos Chagas Filho de Amparo à Pesquisa do Estado do Rio de Janeiro, Conselho Nacional de Desenvolvimento Científico e Tecnológico and the Ministério da Ciência e Tecnologia, the Deutsche Forschungsgemeinschaft and the Collaborating Institutions in the Dark Energy Survey. The DES participants from Spanish institutions are partially supported by MINECO under grants AYA2012-39559, ESP2013-48274, FPA2013-47986, and Centro de Excelencia Severo Ochoa SEV-2012-0234, some of which include ERDF funds from the European Union. This material is based upon work supported by the National Science Foundation under Grant Number (1138766).

The Collaborating Institutions are Argonne National Laboratory, the University of California at Santa Cruz, the University of Cambridge, Centro de Investigaciones Energéticas, Medioambientales y Tecnológicas-Madrid, the University of Chicago, University College London, the DES-Brazil Consortium, the Eidgenössische Technische Hochschule (ETH) Zürich, Fermi National Accelerator Laboratory, the University of Edinburgh, the University of Illinois at Urbana-Champaign, the Institut de Ciències de l'Espai (IEEC/CSIC), the Institut de Física d'Altes Energies, Lawrence Berkeley National Laboratory, the Ludwig-Maximilians Universität and the associated Excellence Cluster Universe, the University of Michigan, the National Optical Astronomy Observatory, the University of Nottingham, The Ohio State University, the University of Pennsylvania, the University of Portsmouth, SLAC National Accelerator Laboratory, Stanford University, the University of Sussex, and Texas A&M University.

Facility: Magellan:I (IMACS).

References

Ackermann, M., Albert, A., Anderson, B., et al. 2015, PhRvL, 115, 231301
Albert, A., Anderson, B., Bechtol, K., et al. 2016, arXiv:1611.03184
An, D., Johnson, J. A., Clem, J. L., et al. 2008, ApJS, 179, 326
Battaglia, G., Tolstoy, E., Helmi, A., et al. 2011, MNRAS, 411, 1013
Bechtol, K., Drlica-Wagner, A., Balbinot, E., et al. 2015, ApJ, 807, 50
Belokurov, V., Zucker, D. B., Evans, N. W., et al. 2007, ApJ, 654, 897
Binney, J., & Tremaine, S. 2008, Galactic Dynamics (2nd ed.; Princeton: Princeton Univ. Press)
Bovy, J., Allende Prieto, C., Beers, T. C., et al. 2012, ApJ, 759, 131
Bradford, J. D., Geha, M., Muñoz, R. R., et al. 2011, ApJ, 743, 167
Bressan, A., Marigo, P., Girardi, L., et al. 2012, MNRAS, 427, 127
Brown, T. M., Tumlinson, J., Geha, M., et al. 2014, ApJ, 796, 91
Carrera, R., Pancino, E., Gallart, C., & del Pino, A. 2013, MNRAS, 434, 1681
Charbonnier, A., Combet, C., Daniel, M., et al. 2011, MNRAS, 418, 1526
Collins, M. L. M., Tollerud, E. J., Sand, D. J., et al. 2017, MNRAS, in press (arXiv:1608.05710)
Contenta, F., Gieles, M., Balbinot, E., & Collins, M. L. M. 2017, MNRAS, 466, 1741
Cooper, M. C., Newman, J. A., Davis, M., Finkbeiner, D. P., & Gerke, B. F. 2012, spec2d: DEEP2 DEIMOS Spectral Pipeline, Astrophysics Source Code Library, ascl:1203.003
Côté, P., Djorgovski, S. G., Meylan, G., Castro, S., & McCarthy, J. K. 2002, ApJ, 574, 783
de Boer, T. J. L., Tolstoy, E., Saha, A., et al. 2011, A&A, 528, A119
Dressler, A., Bigelow, B., Hare, T., et al. 2011, PASP, 123, 288
Dressler, A., Hare, T., Bigelow, B. C., & Osip, D. J. 2006, Proc. SPIE, 6269, 62690F
Drlica-Wagner, A., Albert, A., Bechtol, K., et al. 2015a, ApJL, 809, L4
Drlica-Wagner, A., Bechtol, K., Allam, S., et al. 2016, ApJL, 833, L5
Drlica-Wagner, A., Bechtol, K., Rykoff, E. S., et al. 2015b, ApJ, 813, 109
Essig, R., Sehgal, N., & Strigari, L. E. 2009, PhRvD, 80, 023506
Faria, D., Feltzing, S., Lundström, I., et al. 2007, A&A, 465, 357
Foreman-Mackey, D. 2016, The Journal of Open Source Software, 1, 24
Foreman-Mackey, D., Hogg, D. W., Lang, D., & Goodman, J. 2013, PASP, 125, 306
Frebel, A., Simon, J. D., & Kirby, E. N. 2014, ApJ, 786, 74
Fuhrmann, K., Axer, M., & Gehren, T. 1993, A&A, 271, 451
Geringer-Sameth, A., Koushiappas, S. M., & Walker, M. 2015, ApJ, 801, 74
Hamanowicz, A., Pietrukowicz, P., Udalski, A., et al. 2016, AcA, 66, 197
Harris, W. E. 1996, AJ, 112, 1487
Jethwa, P., Erkal, D., & Belokurov, V. 2016, MNRAS, 461, 2212
Ji, A. P., Frebel, A., Simon, J. D., & Geha, M. 2016, ApJ, 817, 41

Kim, D., & Jerjen, H. 2015, ApJL, 808, L39
Kim, D., Jerjen, H., Geha, M., et al. 2016, ApJ, 833, 16
Kim, D., Jerjen, H., Mackey, D., Da Costa, G. S., & Milone, A. P. 2015a, ApJL, 804, L44
Kim, D., Jerjen, H., Milone, A. P., Mackey, D., & Da Costa, G. S. 2015b, ApJ, 803, 63
Kirby, E. N., Boylan-Kolchin, M., Cohen, J. G., et al. 2013a, ApJ, 770, 16
Kirby, E. N., Cohen, J. G., Guhathakurta, P., et al. 2013b, ApJ, 779, 102
Kirby, E. N., Cohen, J. G., Simon, J. D., & Guhathakurta, P. 2015a, ApJL, 814, L7
Kirby, E. N., Simon, J. D., & Cohen, J. G. 2015b, ApJ, 810, 56
Koch, A., Hansen, T., Feltzing, S., & Wilkinson, M. I. 2014, ApJ, 780, 91
Koch, A., & Rich, R. M. 2014, ApJ, 794, 89
Koposov, S. E., Belokurov, V., Torrealba, G., & Evans, N. W. 2015a, ApJ, 805, 130
Koposov, S. E., Casey, A. R., Belokurov, V., et al. 2015b, ApJ, 811, 62
Koposov, S. E., Gilmore, G., Walker, M. G., et al. 2011, ApJ, 736, 146
Laevens, B. P. M., Martin, N. F., Bernard, E. J., et al. 2015b, ApJ, 813, 44
Laevens, B. P. M., Martin, N. F., Ibata, R. A., et al. 2015a, ApJL, 802, L18
Latham, D. W., Stefanik, R. P., Torres, G., et al. 2002, AJ, 124, 1144
Li, S., Liang, Y.-F., Duan, K.-K., et al. 2016a, PhRvD, 93, 043518
Li, T. S., Simon, J. D., Drlica-Wagner, A., et al. 2016b, ApJ, in press (arXiv:1611.05052)
MAGIC Collaboration 2016, JCAP, 2, 039
Martin, N. F., de Jong, J. T. A., & Rix, H.-W. 2008, ApJ, 684, 1075
Martin, N. F., Geha, M., Ibata, R. A., et al. 2016, MNRAS, 458, L59
Martin, N. F., Nidever, D. L., Besla, G., et al. 2015, ApJL, 804, L5
Martinez, G. D. 2013, arXiv:1309.2641
McConnachie, A. W. 2012, AJ, 144, 4
McConnachie, A. W., & Côté, P. 2010, ApJL, 722, L209
Minor, Q. E., Martinez, G., Bullock, J., Kaplinghat, M., & Trainor, R. 2010, ApJ, 721, 1142
Muñoz, R. R., Majewski, S. R., & Johnston, K. V. 2008, ApJ, 679, 346
Navarro, J. F., Frenk, C. S., & White, S. D. M. 1996, ApJ, 462, 563
Newman, J. A., Cooper, M. C., Davis, M., et al. 2013, ApJS, 208, 5
Peñarrubia, J., Navarro, J. F., & McConnachie, A. W. 2008, ApJ, 673, 226
Preston, G. W., Sneden, C., Thompson, I. B., Shectman, S. A., & Burley, G. S. 2006, AJ, 132, 85
Roederer, I. U., & Sneden, C. 2011, AJ, 142, 22
Sales, L. V., Navarro, J. F., Kallivayalil, N., & Frenk, C. S. 2017, MNRAS, 465, 1879
Santana, F. A., Muñoz, R. R., de Boer, T. J. L., et al. 2016, ApJ, (arXiv:1607.05312)
Simon, J. D., Drlica-Wagner, A., Li, T. S., et al. 2015, ApJ, 808, 95
Simon, J. D., & Geha, M. 2007, ApJ, 670, 313
Simon, J. D., Geha, M., Minor, Q. E., et al. 2011, ApJ, 733, 46
Sobeck, J. S., Kraft, R. P., Sneden, C., et al. 2011, AJ, 141, 175
Sohn, S. T., Majewski, S. R., Muñoz, R. R., et al. 2007, ApJ, 663, 960
Strigari, L. E., Koushiappas, S. M., Bullock, J. S., et al. 2008, ApJ, 678, 614
Tolstoy, E., Irwin, M. J., Helmi, A., et al. 2004, ApJL, 617, L119
Torrealba, G., Koposov, S. E., Belokurov, V., et al. 2016a, MNRAS, 463, 712
Torrealba, G., Koposov, S. E., Belokurov, V., & Irwin, M. 2016b, MNRAS, 459, 2370
Walker, M. G., Mateo, M., Olszewski, E. W., et al. 2006, AJ, 131, 2114
Willman, B., Geha, M., Strader, J., et al. 2011, AJ, 142, 128
Willman, B., & Strader, J. 2012, AJ, 144, 76
Wolf, J., Martinez, G. D., Bullock, J. S., et al. 2010, MNRAS, 406, 1220